The Astrophysical Journal Letters, 966:L27 (10pp), 2024 May 10 https://doi.org/10.3847/2041-8213/ad3bb4

The Kinematic and Chemical Properties of the Close-in Planet Host Star 8 UMi

Huiling Chen[1,2], Yang Huang[3,4,9], Wei Zhu[5], Timothy C. Beers[6,7], Renjing Xie[4], Yutao Zhou[8],
Sharon Xuesong Wang[5], Wei Wang[4], Sofya Alexeeva[4], Qikang Feng[1,2], Haozhu Fu[1,2], Haining Li[4],
Lile Wang[1,2], and Huawei Zhang[1,2,9]
[1] Department of Astronomy, School of Physics, Peking University, Beijing 100871, People's Republic of China; zhanghw@pku.edu.cn
[2] Kavli Institute for Astronomy and Astrophysics, Peking University, Beijing 100871, People's Republic of China
[3] School of Astronomy and Space Science, University of Chinese Academy of Science, Beijing 100049, People's Republic of China; huangyang@ucas.ac.cn
[4] CAS Key Laboratory of Optical Astronomy, National Astronomical Observatories, Chinese Academy of Sciences, Beijing 100101, People's Republic of China
[5] Department of Astronomy, Tsinghua University, Beijing 100084, People's Republic of China
[6] Department of Physics and Astronomy, University of Notre Dame, Notre Dame, IN 46556, USA
[7] Joint Institute for Nuclear Astrophysics—Center for the Evolution of the Elements (JINA-CEE), USA
[8] College of Mathematics and Physics, Guangxi Minzu University, Nanning 530006, People's Republic of China

Received 2024 January 10; revised 2024 April 2; accepted 2024 April 8; published 2024 May 2

Abstract

A recent study by Hon et al. reported that a close-in planet around the red clump star, 8 UMi, should have been engulfed during the expansion phase of its parent star's evolution. They explained the survival of this exoplanet through a binary-merger channel for 8 UMi. The key to testing this formation scenario is to derive the true age of this star: is it an old "imposter" resulting from a binary merger, or a genuinely young red clump giant? To accomplish this, we derive kinematic and chemical properties for 8 UMi using astrometric data from Gaia DR3 and the element-abundance pattern measured from a high-resolution ($R \sim 75{,}000$) spectrum taken by SOPHIE. Our analysis shows that 8 UMi is a normal thin-disk star with orbital rotation speed of $V_\phi = 244.96$ km s^{-1}, and possesses a solar metallicity ($[\mathrm{Fe/H}] = -0.05 \pm 0.07$) and α-element-abundance ratio ($[\alpha/\mathrm{Fe}] = +0.01 \pm 0.03$). By adopting well-established relationships between age and space velocities/elemental abundances, we estimate a kinematic age of $3.50^{+3.00}_{-2.00}$ Gyr, and a chemical age of $3.25^{+2.50}_{-1.50}$ Gyr from [C/N] and 3.47 ± 1.96 Gyr from [Y/Mg] for 8 UMi, respectively. These estimates are consistent with the isochrone-fitting age ($1.90^{+1.15}_{-0.30}$ Gyr) of 8 UMi, but are all much younger than the timescale required in a binary-merger scenario. This result challenges the binary-merger model; the existence of such a closely orbiting exoplanet around a giant star remains a mystery yet to be resolved.

Unified Astronomy Thesaurus concepts: Planet hosting stars (1242); Chemical abundances (224); Stellar evolution (1599); Galaxy kinematics (602)

1. Introduction

Since the first detections of exoplanets (Wolszczan & Frail 1992; Mayor & Queloz 1995), over 5000 exoplanets have been discovered.[10] This extensive sample has revolutionized our knowledge of the formation and evolution of planets (e.g., Zhu & Dong 2021). While the majority of confirmed exoplanets are found around main-sequence stars, planets around evolved stars (see Döllinger & Hartmann 2021 and references therein), or even around stellar remnants (e.g., Wolszczan & Frail 1992), have also been detected. These exotic planets provide useful constraints on the long-term evolution of planetary systems.

The planetary system around the red giant 8 UMi was first discovered by Lee et al. (2015). The mass and eccentricity of the planet, Halla, were determined using the radial-velocity method with high-resolution spectra acquired with the fiber-fed Bohyunsan Observatory Echelle Spectrograph (BOES) mounted on the 1.8 m telescope at Bohyunsan Optical Astronomy Observatory (BOAO). The atmospheric parameters of the host star were also carefully derived from these high-resolution spectra. This discovery is further confirmed by Hon et al. (2023), based on 135 additional radial-velocity measurements using the HIRES spectrograph installed on the Keck I telescope on Maunakea, Hawaii. The semimajor axis of Halla is only 0.462 ± 0.006 au, calculated from fits to its radial-velocity curve; its mass has been estimated from asteroseismology. The measured period spacing $\Delta\Pi$ from asteroseismology suggests that 8 UMi is a helium-burning red clump giant star (Yu et al. 2018). Given these properties, Halla should have been engulfed and destroyed by 8 UMi during the penultimate phase of its evolution, the tip of the red giant branch, when the star expanded out to 0.7 au. To avoid the engulfment of Halla, Hon et al. (2023) proposed a binary-merger formation scenario for 8 UMi. According to their binary evolution model, a close binary composed of two lower-mass stars was required to form a 8 UMi–like red clump star. If this scenario were correct, 8 UMi would be old (∼8.6 Gyr according to the binary-merger model in Hon et al. 2023), and inherit the kinematic and chemical properties from its progenitor binary system. It should belong to the Milky Way's thick-disk population, given the evolution timescale required in the binary-merger model.

In order to check the aforementioned binary-merger scenario, it is crucial to constrain the age of the system. In this Letter, the kinematic and chemical properties of the host star 8 UMi are carefully investigated using astrometric data

---

[9] Corresponding authors.

[10] https://exoplanetarchive.ipac.caltech.edu/

from Gaia DR3 (Gaia Collaboration et al. 2023) and a high-resolution ($R \sim 75{,}000$) spectrum from the SOPHIE archive.[11] This information is used to derive the kinematic and chemical ages of 8 UMi, based on well-established relations between age and space velocities/chemical elemental-abundance ratios. In Section 2, we briefly introduce the adopted data and the analysis of high-resolution spectrum. Section 3 presents the mass, age, measurements of 3D positions, 3D space velocities, and the chemical-abundance pattern of 8 UMi. Kinematic and chemical constraints on the true age of 8 UMi are also provided. Based on these results, we conclude that the binary-merger scenario is unlikely, and that alternative explanations must be considered for the 8 UMi system. Section 4 presents a brief summary.

2. Data and Spectrum Analysis

2.1. Gaia DR3

In this study, the astrometric parameters and the broadband photometry of 8 UMi are retrieved from Gaia DR3[12] (Gaia Collaboration et al. 2023). The derived distance of 8 UMi is 163.7 ± 0.4 pc, measured from the Gaia parallax with the zero-point corrected (Lindegren et al. 2021; Huang et al. 2021a). To correct for the reddening, the value of extinction $E(B-V) = 0.02$ is taken from the reddening map of Schlegel et al. (1998), with systematics corrected. The extinction coefficients of the three Gaia bands are taken from Table 1 of Huang et al. (2021b). The intrinsic color and absolute magnitude of 8 UMi are thus $(B_P - R_P)_0 = 1.13 \pm 0.03$ and $M_G = 0.45 \pm 0.05$, respectively. The uncertainties are from the photometric errors and the reddening correction by assuming a constant error of 0.02 in $E(B-V)$.

2.2. High-resolution Spectrum and Analysis

Analysis of a high-resolution spectrum is required to accurately infer the elemental-abundance ratios of 8 UMi. We searched for observation records in public spectral data archives, and retrieved the high-resolution spectrum of 8 UMi from the SOPHIE archive. This spectrum was obtained with the 1.93 m telescope at Haute Provence Observatory equipped with the SOPHIE échelle spectrograph. The downloaded spectrum is processed through the standard data reduction pipeline of SOPHIE. First, a two-dimensional spectrum (E2DS) is obtained after optimal order extraction, cosmic-ray extraction, wavelength calibration, and spectral flat-field correction to the raw data. Second, the pipeline merges the 39 spectral orders after correction of the blaze function, yielding a one-dimensional spectrum (S1D; Bouchy et al. 2009). The observation mode employed for 8 UMi was the high-resolution mode (HR mode), with a spectral resolution of $R \sim 75{,}000$, covering the wavelength range from 3872 to 6943 Å. The signal-to-noise ratio (S/N) of this spectrum is generally above 100 (peak S/N ~350 at around 6300 Å), except at the very blue edge ($\leqslant$4050 Å), which is excluded in the following analysis.

For the downloaded spectrum, we use the cross-correlation function method to calculate its line-of-sight velocity $v_{\rm los} = -9.58 \pm 0.03$ km s^{-1}. The spectrum is corrected to the rest frame using the derived $v_{\rm los}$, and then is normalized locally by division with a pseudo-continuum defined manually. To derive atmospheric parameters (i.e., effective temperature $T_{\rm eff}$, surface gravity $\log g$, and metallicity [Fe/H]) of 8 UMi, we employ the equivalent width (EW) method with the MOOG radiative transfer code (Sneden et al. 2012). The MARCS atmospheric model (Gustafsson et al. 2008), the line list compiled from Chen et al. (2000) and Sitnova et al. (2015), and the solar abundance of Grevesse et al. (2007) are adopted. All of these processing steps are combined in the integrated software package iSpec (Blanco-Cuaresma 2019). The EWs of the atomic iron lines are measured, based on the compiled line list mentioned above. Specifically, a Gaussian function is adopted to fit unblended single atomic absorption lines. Ultimately, the EWs of 30 Fe I lines and 7 Fe II well separated and weak to mild-strength lines (20–100 mÅ) are measured in this way.

The measured EWs, using $T_{\rm eff} = 4847$ K, $[{\rm Fe/H}] = -0.03$, and $v_{\rm mic} = 1.30$ km s^{-1} from Hon et al. (2023) as an initial guess, are employed to derive the atmospheric parameters of 8 UMi using the nonlinear least-squares fitting algorithm installed in iSpec, which considers both excitation equilibrium and ionization balances. For surface gravity, we have two estimates: one, $\log g = 2.57$, is from the asteroseismologic scaling relation (Kallinger et al. 2018) with maximum power $\nu_{\rm max}$ measured by Hon et al. (2023) from TESS, with a correction for a ~4% systematic offset found in Stello et al. (2022); another, $\log g = 2.63$, is from isochrone fitting based on the Bayesian technique (see Section 3.1 for details). A mean value of $\log g = 2.60$ is the input value in iSpec for $\log g$; it changes slightly with the changes of $T_{\rm eff}$ and [Fe/H] during the iteration. Finally, the atmospheric parameters are found to be $T_{\rm eff} = 4897 \pm 100$ K, $\log g = 2.60 \pm 0.07$, $[{\rm Fe/H}] = -0.05 \pm 0.07$, and $v_{\rm mic} = 1.48 \pm 0.10$ km s^{-1}. Figure 1 shows the [Fe/H] estimates as a function of reduced EWs and excitation potential. The slopes between [Fe II and I/H] and reduced EW/excitation potential are both flat.[13] The difference between [Fe I/H] and [Fe II/H] is smaller than 0.01 dex. In general, the derived atmospheric parameters are consistent with those from Hon et al. (2023), as well as those estimated in the original discovery paper (Lee et al. 2015).

Based on the estimated atmospheric parameters, the chemical abundances for a total of 23 elements are measured using the software packages SIU (Reetz 1991) and TAME (Kang & Lee 2012) by the spectrum-synthesis method with the assumption of LTE. A differential analysis is adopted when deriving abundances. The original atomic parameters are from different sources for different elements. The atomic parameters for the CH molecular lines are taken from Masseron et al. (2014). The line list is generated using LINEMAKE (Placco et al. 2021) around 4215 Å for deriving the abundance of N. For other elements, the atomic parameters are drawn from several studies including Neves et al. (2009), Zhao et al. (2016), and Sitnova et al. (2022). We refine the $\log gf$ values of each atomic line to make sure they well reproduce atomic absorption-line profiles in the solar spectrum of Kurucz et al. (1984). The refined $\log gf$ values, excitation potentials, EWs observed in the solar spectrum, EWs measured in 8 UMi, and the corresponding abundances calculated for 8 UMi of individual lines are presented in Table A1. Synthetic line-fitting examples for CH, CN, Mg, and Y in 8 UMi are shown in

---

[11] http://atlas.obs-hp.fr/sophie/

[12] https://gea.esac.esa.int/archive/

[13] For excitation balance, a not significant slope of 0.015 dex eV^{-1} is detected.

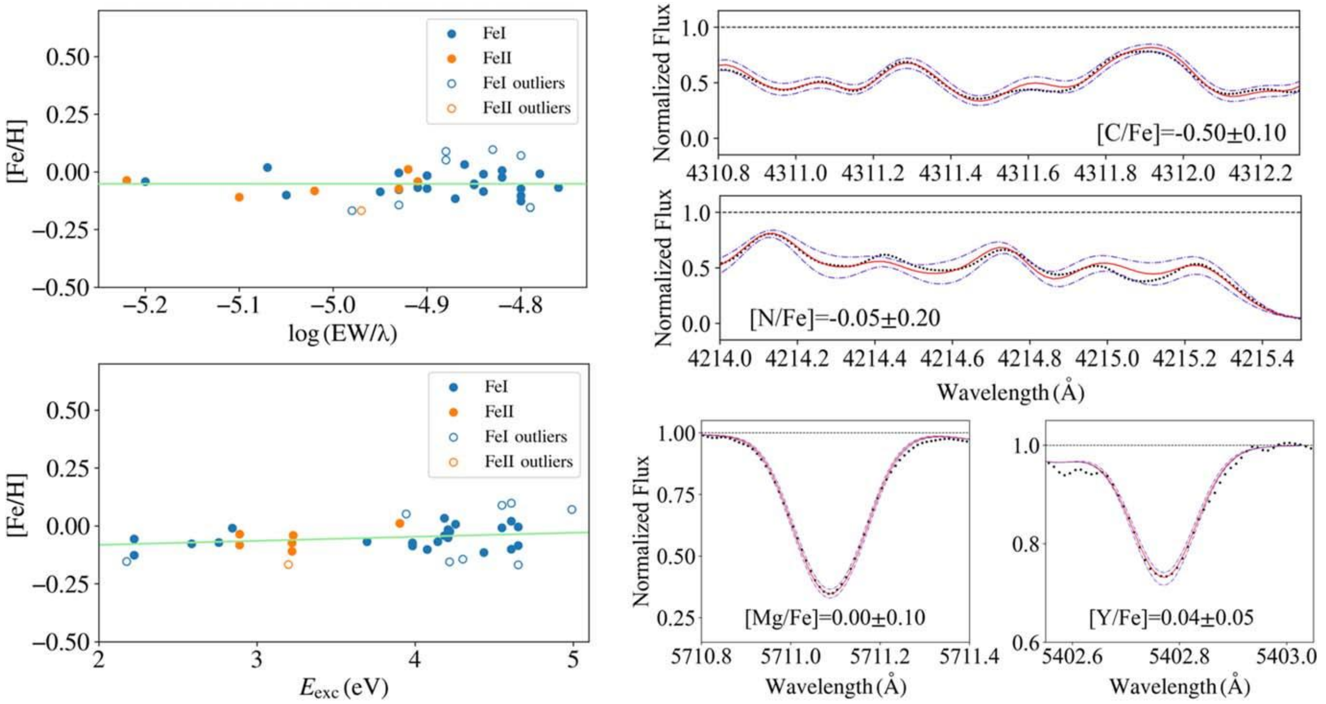

Figure 1. Left panels: [Fe/H] estimates as a function of reduced equivalent width (upper subpanel) and excitation potential (lower subpanel). The open circles represent the lines filtered by the sigma-clipping process of iSpec with a 0.90 weight scale. Right panels: synthetic spectrum-fitting examples (red solid line) of 8 UMi in the abundance-determination process. The black dots show the observed spectrum. The upper two subpanels show portions of the CH and CN bands with 1σ errors (blue dashed–dotted line). The lower two subpanels show the fitting examples for the Mg 5711 Å and Y 5402 Å lines, with abundance variations for 0.10 and 0.05 dex, respectively.

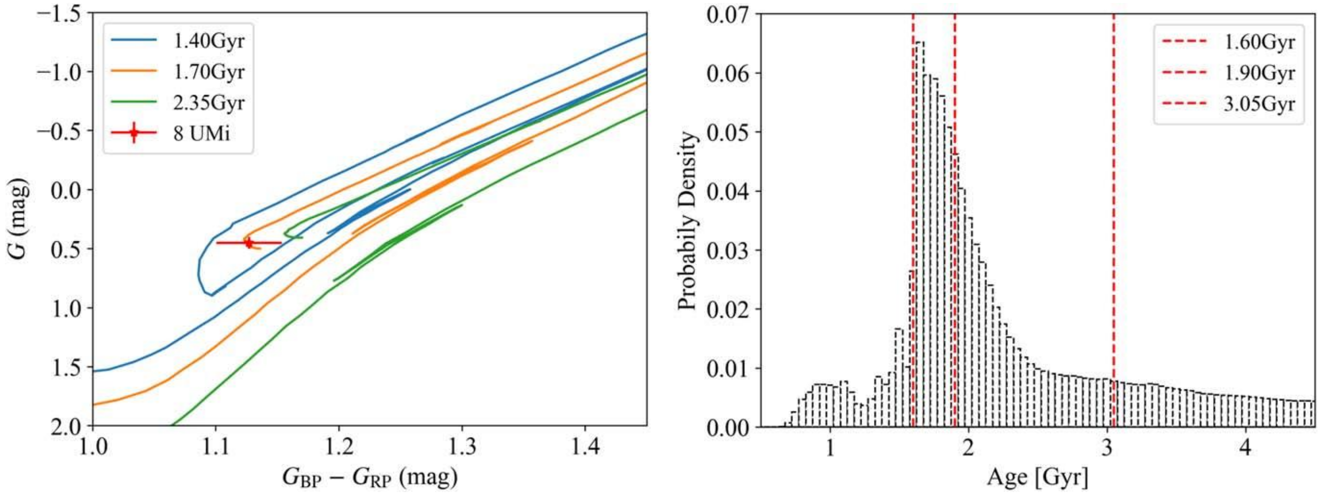

Figure 2. Left panel: theoretical isochrones of 1.40, 1.70, and 2.35 Gyr (from left to right) and [M/H] = −0.05 in the $(B_{\rm P}-R_{\rm P})_0$–$M_{\rm G}$ diagram. The red star with error bars represents 8 UMi. Right panel: the posterior probability density distribution of age calculated by our Bayesian method (see Section 3.1). The red dashed lines of 1.60, 1.90, and 3.05 Gyr represent the 16%, 50%, and 84% cumulative probability levels.

Figure 1. For the solar spectrum, the synthetic line-fitting results are presented in Figure A1.

3. Results and Discussion

3.1. Mass and Age from Isochrone Fitting

To derive the mass and age of 8 UMi, we adopt a conventional Bayesian method, similar to that developed in Huang et al. (2022), by matching the observed stellar parameters with theoretical isochrones. The theoretical isochrones are taken from PARSEC (Bressan et al. 2012), with [M/H] from −0.12 to +0.02 in steps of 0.01 dex, and age from 0.5 to 4.5 Gyr in steps of 0.05 Gyr. The full grids include over 540,000 individual models. The input observable constraints are intrinsic color $(B_{\rm P}-R_{\rm P})_0$ and absolute magnitude M_G (see Section 2.1). As an example, Figure 2 compares 8 UMi to model isochrones in the M_G–$(G_{\rm BP}-G_{\rm RP})_0$ diagram (left panel), and presents the posterior probability distribution function (PDF) of age yielded by the Bayesian estimate (right panel). Based on the PDF, the age of 8 UMi is

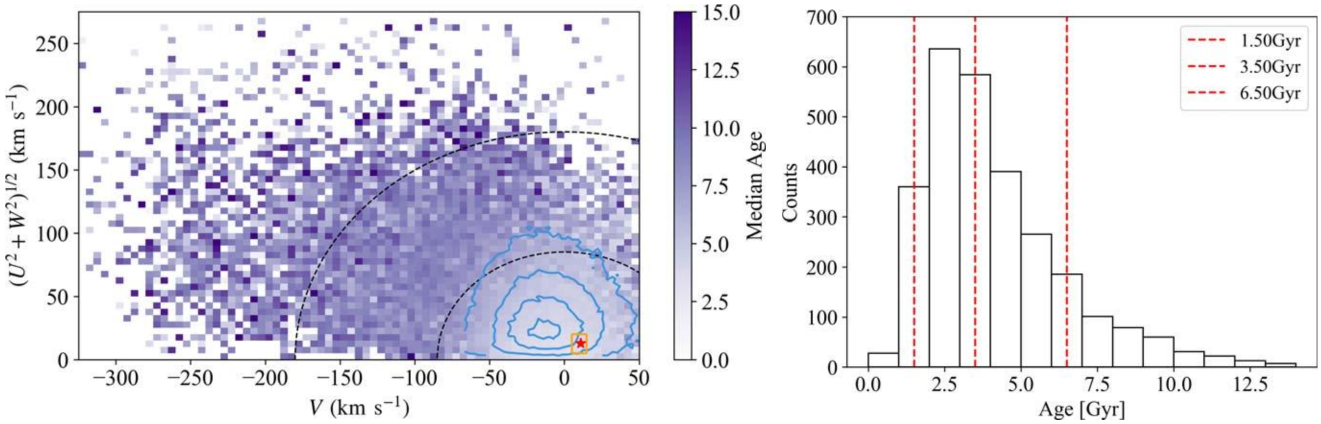

Figure 3. Left panel: Toomre diagram for 8 UMi (red star). Overplotted background is the distribution of field red clump stars from Huang et al. (2020), color coded by median age with the color bar shown on the right side. The bin size is 5 and 5 km s^{-1} in the X-axis and Y-axis, respectively. The two dashed circles delineate constant total space velocities with respect to the local standard of rest of $V_{\rm tot} = 85$ and 180 km s^{-1}, respectively, as commonly used to define a sample of thick-disk stars. The blue contours represent the 10%, 50%, 84%, and 99% of the thin-disk population selected from the field red clump stars, based on the criteria taken from Chen et al. (2021). The red rectangle (V from 5 to 15 km s^{-1} and $\sqrt{U^2 + W^2}$ from 5 to 20 km s^{-1}) selects stars with similar 3D space velocities to 8 UMi. Right panel: the age distribution of the red clump stars selected by the red rectangle shown in the left panel. Lines of 1.50, 3.50, and 6.50 Gyr mark the 16%, 50%, and 84% cumulative probabilities, respectively.

found to be $\tau = 1.9^{+1.2}_{-0.3}$ Gyr. The upper and lower uncertainties correspond to the 16% and 84% percentiles of the resulting PDF. This suggests 8 UMi is a young star, if it has evolved as a single star.

The isochrone fitting yields a mass of $1.70^{+0.15}_{-0.25}\,M_\odot$ for 8 UMi. This is consistent with the stellar mass derived in a similar way by the original planet discovery paper (Lee et al. 2015), but larger by 13% than the asteroseismic measurement ($1.51 \pm 0.05\,M_\odot$) of Hon et al. (2023). We do not attempt to resolve this discrepancy here, but note that the asteroseismic measurements on 8 UMi by two different studies, Hon et al. (2023) and Hatt et al. (2023), are inconsistent with each other in the oscillation frequency at the maximum power, $\nu_{\rm max}$, which is the key parameter that determines the stellar mass. These two studies both used TESS data, although they differ in the number of sectors (8 versus 12). According to Hatt et al. (2023), the oscillation frequency at the maximum power, $\nu_{\rm max}$, is determined to be $50.8 \pm 2.4\,\mu$Hz, which would suggest a host mass of about $2\,M_\odot$.

The value of the host star mass may be the key to resolve the puzzle of 8 UMi b. A higher host mass means that the planetary orbit is slightly wider at a given orbital period. In the mass range 1.5–2.0 $M_\odot$, a higher mass also produces a smaller stellar size at the tip of red giant branch. The latter is best illustrated in the panel (b) of Figure 3 in Hon et al. (2023) for the case of the 8 UMi system. As a consequence, the impact of the tidal effect also sensitively depends on the host star mass, and a slightly higher mass can reduce the chance of planet engulfment during the red giant branch (RGB) and helium-flash phases, as theoretical studies have shown (e.g., Kunitomo et al. 2011).

3.2. Space Velocities and Kinematic Age

The Gaia DR3 astrometric information and distance estimate (see Section 2.1), as well as the radial velocity measured from the SOPHIE spectrum (see Section 2.2), are adopted to derive space velocities with the `galpy` python package (Bovy 2015). For this calculation, the solar motions are set to be ($U_\odot$, $V_\odot$, $W_\odot$) = (−7.01, 10.13, 4.95) km s^{-1} (Huang et al. 2015), and the circular speed at the solar position set to be $V_c(R_0) = 234.04$ km s^{-1} from Zhou et al. (2023). For the solar positions, we adopt a value of $R_0 = 8.178$ kpc (GRAVITY Collaboration et al. 2019) for the Galactocentric distance, and a value of $Z_0 = 25$ pc (Bland-Hawthorn & Gerhard 2016) for the vertical offset. The resulting space velocity components of 8 UMi are $(U, V, W) = (-10.28 \pm 0.20, 10.92 \pm 0.12, -7.61 \pm 0.09)$ km s^{-1} in a Cartesian coordinate system centered on the Sun and $(V_R, V_\phi, V_Z) = (-10.28 \pm 0.20, 244.96 \pm 0.19, -7.61 \pm 0.09)$ km s^{-1} in Galactocentric cylindrical coordinates. The three-dimensional positions of 8 UMi are $R = 8.228 \pm 0.035$ kpc, $\phi = 0^\circ\!.809 \pm 0^\circ\!.004$, and $Z = 129.7 \pm 0.5$ pc. Errors in the space velocities and positions are calculated by 20,000 Monte Carlo simulations by sampling the measurement errors (assuming Gaussian distributions). Figure 3(a) shows the location of 8 UMi in the Toomre diagram. For comparison, the background shows the distribution of field red clump giant stars (sample taken from Huang et al. 2020) color coded by median age. In Huang et al. (2020), the ages of these red clump stars are estimated from LAMOST spectra, using machine-learning techniques, with the ages calibrated using asteroseismic masses from Kepler. The typical age uncertainty is 20%. In this figure, we also show density contours of the thin-disk population selected from the field red clump sample with the criteria from Chen et al. (2021). 8 UMi falls on the typical position of members of the thin-disk population with young median ages.

To provide a quantitative estimate of the kinematic age for 8 UMi, red clump stars with 3D space velocities similar to 8 UMi (i.e., V between 5 and 15 km s^{-1} and $\sqrt{U^2 + W^2}$ between 5 and 20 km s^{-1}) are selected. The right panel of Figure 3 shows the age distribution of those selected red clump stars. This leads to an kinematic age estimate $\tau_{\rm kinematic} = 3.5^{+3.0}_{-2.0}$ Gyr for 8 UMi.

3.3. Elemental-abundance Pattern and Chemical Age

Table 1 presents the chemical-abundance pattern for 8 UMi determined using the methods described in Section 2.2. The errors of the derived abundances are also provided in Table 1. The values of σ represent the statistical uncertainties in measurements, while the δ[X/Fe] represents the systematic error estimated from changes of abundances by individually varying $T_{\rm eff}$, $\log g$, [Fe/H], and $v_{\rm mic}$ according to the 1σ

Table 1

Elemental-abundance Ratios of 23 Elements for 8 UMi[a]

Element	[X/Fe]	σ[b] (dex)	N[c]	δ[X/Fe]			
				$\delta T = \pm 100$ K	$\delta \log g = \pm 0.07$	δ[Fe/H] $= \pm 0.07$	$\delta v_{\mathrm{mic}} = \pm 0.10$ km s^{-1}
C	−0.50	0.10	⋯	$\pm$0.10	$\pm$0.05	$\pm$0.10	$\mp$0.02
N	−0.05	0.20	⋯	$\pm$0.08	$\pm$0.02	$\mp$0.05	$\mp$0.02
O	−0.18	0.07	1	$\mp$0.07	$\pm$0.04	$\mp$0.05	0.00
Na	+0.27	0.02	2	$\pm$0.08	0.00	$\mp$0.07	$\mp$0.02
Mg	+0.02	0.03	2	$\pm$0.07	$\mp$0.02	$\mp$0.07	$\mp$0.03
Al	+0.16	0.01	2	$\pm$0.07	0.00	$\mp$0.07	$\mp$0.02
Si	+0.02	0.01	5	$\mp$0.02	$\pm$0.01	$\mp$0.07	$\mp$0.01
Ca	0.00	0.02	6	$\pm$0.10	0.00	$\mp$0.08	$\mp$0.04
Sc	−0.16	0.05	5	$\pm$0.01	$\pm$0.03	$\mp$0.07	$\mp$0.04
Ti	−0.01	0.05	6	$\pm$0.09	$\pm$0.01	$\mp$0.07	$\mp$0.03
V	+0.07	0.07	5	$\pm$0.17	0.00	$\mp$0.07	$\mp$0.03
Cr	−0.03	0.08	4	$\pm$0.12	$\pm$0.01	$\mp$0.08	$\mp$0.03
Mn	+0.07	0.04	2	$\pm$0.09	$\pm$0.01	$\mp$0.09	$\mp$0.03
Co	−0.03	0.05	3	$\pm$0.06	$\pm$0.01	$\mp$0.07	$\mp$0.01
Ni	−0.09	0.05	5	$\pm$0.05	$\pm$0.01	$\mp$0.07	$\mp$0.03
Zn	−0.29	0.07	1	$\mp$0.02	$\pm$0.02	$\mp$0.07	$\mp$0.06
Y	+0.06	0.03	2	0.00	$\pm$0.04	$\mp$0.06	$\mp$0.02
Zr	0.00	0.07	1	0.00	$\pm$0.04	$\mp$0.07	$\mp$0.01
Ba	+0.25	0.06	3	$\pm$0.04	$\pm$0.01	$\mp$0.06	$\mp$0.08
La	+0.30	0.07	1	$\pm$0.02	$\pm$0.03	$\mp$0.05	$\mp$0.01
Nd	+0.31	0.04	2	$\pm$0.03	$\pm$0.03	$\mp$0.06	$\mp$0.02
Eu	+0.15	0.07	1	$\mp$0.01	$\pm$0.03	$\mp$0.06	$\mp$0.01
A(Li)[d]	1.94	0.07	1	$\pm$0.15	0.00	$\mp$0.07	0.00

Notes.

[a] The abundance ratios are derived using the atmospheric parameters: $T_{\mathrm{eff}} = 4897 \pm 100$ K, $\log g = 2.60 \pm 0.07$, [Fe/H] $= -0.05 \pm 0.07$, $v_{\mathrm{mic}} = 1.48 \pm 0.10$ km s^{-1} (see Section 2.2 for details).

[b] σ represents the statistical uncertainties in measurements. For elements with more than two lines, it is calculated from the scatter of the abundances derived from all lines. For elements with only one line (O, Li, Zn, Zr, La, Eu), the statistical error of [Fe/H] is adopted. As for C and N, we adopt the 1σ uncertainty as shown in the left panel of Figure 1.

[c] N represents the number of atomic absorption lines used to derive the chemical abundance.

[d] We adopted a solar abundance $A(\mathrm{Li})_{\odot} = 1.01$ taken from Grevesse et al. (2007).

parameter uncertainties. Overall, the chemical results indicate that 8 UMi, with [Fe/H] $= -0.05 \pm 0.07$ and [α/Fe] $= +0.01 \pm 0.03$, is a typical thin-disk star. In addition, four intriguing features are also seen in the chemical-abundance pattern of 8 UMi. First, the lithium abundance is significantly enhanced, with $A(\mathrm{Li}) \approx 1.94$, which is consistent with previous measurements of $A(\mathrm{Li}) = 2.0 \pm 0.2$ from Kumar et al. (2011) and Charbonnel et al. (2020). Possible origins of this enhanced Li abundance are discussed in the next section. Second, the carbon abundance is relatively low for such a solar-metallicity star. It may be attributed to extra mixing through the CNO cycle (aka the first dredge-up process) during the RGB phase (e.g., Boothroyd & Sackmann 1999). Third, [Zn/Fe] $= -0.29$ is slightly lower than the solar value. Note that Sitnova et al. (2022) reported a median [Zn/Fe] ≈ -0.10, with a lower boundary extending as low as −0.30, for thin-disk stars with solar metallicity. This suggests that subsolar zinc abundances are quite common for solar-metallicity stars. Finally, the s-process elements (Ba, La, Nd) exhibit slightly higher abundances, with an average value of [X/Fe] $\approx +0.20$ to +0.30. This supersolar abundance is additional evidence for the genuinely young age for 8 UMi, since the fraction of s-process elements increases with time in the Universe (Spina et al. 2018).

As mentioned above, the [C/N] ratio at the stellar surface is potentially influenced by the CNO cycle during the first dredge-up, which is correlated with the stellar mass. Thus, [C/N] is a good age indicator for giants because of the mass–age relation in stellar evolution. The left panel of Figure 4 shows the [C/N]-age distribution, using red clump stars again from Huang et al. (2020). The [Fe/H] range of this sample is from −1.0 to +0.5. Their [C/H] and [N/H] are derived from LAMOST low-resolution spectra by adopting a machine-learning method using the LAMOST-APOGEE stars in common as a training sample. The typical precision of the derived [C/H] and [N/H] is about 0.1 dex. We determine $\tau_{[\mathrm{C/N}]} = 3.3^{+2.5}_{-1.5}$ Gyr for 8 UMi based on the age distribution of red clump stars with [C/N] ranging from −0.67 to −0.23, the 1σ interval on [C/N] measured for 8 UMi (see Table 1). The systematic error of [C/N] measurement is about 0.15 dex; its effect on age estimate is around 1.5 Gyr.

Over the last decade, the ratios between s-process and α-elements have been found to be chemical clocks for solar-metallicity stars. Among all the ratios, the [Y/Mg]–age relation is tight and applicable for both dwarf and giant stars (e.g., Nissen et al. 2020; Casamiquela et al. 2021). By fitting a linear relation[14] for age–[Y/Mg] based on a nearby sample[15] from Nissen et al. (2020), the age inferred from [Y/Mg] for 8 UMi is $\tau_{[\mathrm{Y/Mg}]} = 3.5 \pm 2.0$ Gyr. The uncertainty is given by the 1σ

---

[14] [Y/Mg] $= 0.166$–$0.0362 \times \tau$.

[15] This sample includes 72 nearby stars with element abundances measured from high-resolution and S/N spectra, and age uncertainties between 0.5 and 1.3 Gyr.

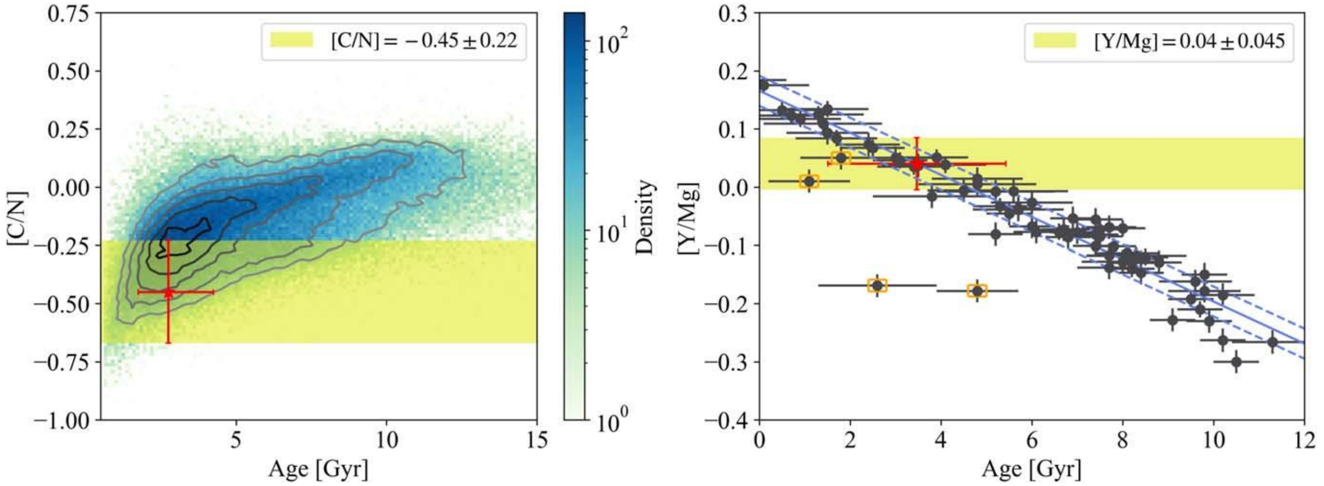

Figure 4. Left panel: density map for age estimates based on [C/N], using red clump stars taken from Huang et al. (2020). The yellow horizontal region marks the measurement of [C/N] for 8 UMi. The age of 8 UMi is calculated from the probability distribution of the crossed region; the red star indicates the final derived age for 8 UMi. Right panel: the age–[Y/Mg] relation using nearby 72 nearby stars (black dots) taken from Nissen et al. (2020). The blue solid line and dashed lines are the least-squares linear fit and 1σ error for the sample stars. Two binaries and two Na-rich stars are excluded in the fitting (labeled by orange rectangles in the figure; see Section 4.4 of Nissen et al. 2020 for details). The yellow horizontal region marks the measurement of [Y/Mg] for 8 UMi. The red star represents 8 UMi, with age given by the linear relation and errors from the uncertainty of the linear relation and measurement errors of [Y/Mg].

uncertainty of the linear relation and the measurement error of [Y/Mg]. The systematic error, resulting from varying stellar atmospheric parameters and $v_{\rm mic}$ (see Table 1), amounts to 0.09 dex, corresponding to an uncertainty of 2.5 Gyr in age. Moreover, we investigate the NLTE effects on Mg and Y. In the model atmosphere of 4897/2.60/−0.05, the NLTE calculations were conducted for Mg I and Y II using the model atoms detailed in Alexeeva et al. (2018, 2023). The NLTE abundance corrections, represented as $\Delta_{\rm NLTE} = \log\,\epsilon_{\rm NLTE} - \log\,\epsilon_{\rm LTE}$, for the Mg I lines at 5528 and 5711 Å are 0.00 and +0.03 dex, respectively. Similarly, for the Y II lines at 5289 and 5402 Å, the corrections are +0.01 and 0.00 dex, respectively. Thus, the systematic error induced by NLTE effects (−0.01 dex) is negligible comparing to the one caused by errors in the stellar atmospheric parameters and $v_{\rm mic}$.

In summary, the ages of 8 UMi derived from the two chemical clocks agree very well with each other. The chemical ages are also consistent with that derived from the kinematic estimate in Section 3.2.

3.4. Is 8 UMi Formed through a Merger?

According to Hon et al. (2023), an old age[16] is required for the binary-merger formation channel of 8 UMi. However, the above kinematic and chemical results show that the true age of this system is 3.25–3.50 Gyr, with a 1σ statistical uncertainty of 1.50–3.00 Gyr. This is consistent with the isochrone-fitting age of $1.9^{+1.2}_{-0.3}$ Gyr derived under the single-star assumption.

Another argument that was used in Hon et al. (2023) to support the binary-merger scenario is that such a formation channel can explain the Li enhancement of 8 UMi. Previous studies have shown that most recognized Li-rich giants are found among the red clump stars (e.g., Yan et al. 2021). To explain this Li enhancement in red clump stars, one possible scenario is the merger of a HeWD and an RGB that triggers a convection shell to synthesize Li, leading to Li-rich red clump stars (Zhang et al. 2020). However, other competing models that do not invoke binary mergers can also produce Li-rich red clump stars, such as planet engulfment (Aguilera-Gómez et al. 2016) and the lithium enhancement in the tip of the RGB process or in the helium flash (Silva Aguirre et al. 2014). Given that there is another giant planet with a relatively wide orbit in 8 UMi, the chance is high that one or several small planets may have existed on inner orbits (Zhu & Dong 2021), and the ingestion of such close-in planets would be sufficient to explain the observed Li abundance (e.g., Aguilera-Gómez et al. 2016).

In summary, the binary-merger formation channel of 8 UMi proposed by Hon et al. (2023) is not supported by our kinematic and chemical analysis of 8 UMi. Alternative models are required to explain the existence of the close-in planet Halla orbiting 8 UMi.

4. Conclusions

Using astrometric data from Gaia DR3 and a high-resolution spectrum from the SOPHIE archive, we determine the mass, age, 3D position, space velocity, and the chemical-abundance pattern for 8 UMi. Our results reveal that the planet's host star 8 UMi is a single middle-aged thin-disk star with a normal orbital rotation speed of $V_\phi = 244.96$ km s^{-1}. It also exhibits a solar-like metal abundance and [α/Fe] ratio. To test the binary-merger formation scenario for 8 UMi, we have determined its age by different methods, including isochrone-fitting assuming a single-star evolution, and kinematic and chemical age estimates from well-established age–space velocities/chemical element-abundance relations. The four derived ages are

1) Isochrone age: $\tau_{\rm isochrone} = 1.9^{+1.2}_{-0.3}$ Gyr;
2) Kinematic age: $\tau_{\rm kinematic} = 3.5^{+3.0}_{-2.0}$ Gyr;
3) [C/N] age: $\tau_{\rm [C/N]} = 3.3^{+2.5}_{-1.5}$ Gyr;
4) [Y/Mg] age: $\tau_{\rm [Y/Mg]} = 3.5 \pm 2.0$ Gyr.

These age measurements consistently suggest that 8 UMi is a middle-aged star formed approximately 2–4 Gyr ago. This is much younger than the timescale that is needed to go though the binary-merger process of Hon et al. (2023). Further investigations are needed to fully resolve the puzzle of the 8 UMi planetary system.

---

[16] 8.6 Gyr is required in their example binary-evolutionary model.

Acknowledgments

This work is funded by the National Key R&D Program of China (No. 2019YFA0405500) and the National Natural Science Foundation of China (NSFC grant Nos. 12090040, 12090044, 11833006, 12133005, 12173021, and 11833002). T.C.B. acknowledges partial support for this work from grant PHY 14-30152; Physics Frontier Center/JINA Center for the Evolution of the Elements (JINA-CEE), and OISE-1927130: The International Research Network for Nuclear Astrophysics (IReNA), awarded by the US National Science Foundation. W.Z. is also supported by the CASSACA grant CCJRF2105.

Thanks to the maintenance of the SOPHIE data archive by Haute Provence Observatory (http://atlas.obs-hp.fr/sophie/) we were able to obtain access to the high-resolution spectrum used in this study. We also used data from the European Space Agency mission Gaia (https://www.cosmos.esa.int/Gaia), processed by the Gaia Data Processing and Analysis Consortium (DPAC; see http://www.cosmos.esa.int/web/Gaia/dpac/consortium). Besides, this research has made use of the NASA Exoplanet Archive (https://exoplanetarchive.ipac.caltech.edu/), which is operated by the California Institute of Technology, under contract with the National Aeronautics and Space Administration under the Exoplanet Exploration Program.

Appendix

Line Data and Synthetic Fitting Examples in the Solar Spectrum

This appendix contains detailed line data for all of the lines used in our abundance analysis (Table A1) and the examples of synthetic fitting in the solar spectrum when doing differential analysis (Figure A1).

Table A1

Line Data Used in the Abundance Derivation

Atom	λ (Å)	E_{exc} (eV)	log *gf*	EW$_{\odot}$ (mÅ)	EW$_{8\ \mathrm{UMi}}$ (mÅ)	[X/Fe]$_{8\ \mathrm{UMi}}$ (dex)
Li	6707.80	0.17	0.00	⋯	138.11	+0.98
O	6300.30	0.00	−9.58	7.65	32.16	−0.18
Na	6154.23	2.10	−1.58	37.92	72.79	+0.28
Na	6160.75	2.10	−1.26	59.40	95.42	+0.25
Mg	5528.00	4.34	−0.47	237.72	227.83	+0.04
Mg	5711.09	4.34	−1.70	107.42	130.84	0.00
Al	6696.02	3.14	−1.55	38.00	66.36	+0.16
Al	6698.67	3.14	−1.90	21.84	45.59	+0.18
Si	6142.48	5.62	−1.50	34.14	42.52	+0.01
Si	6145.02	5.62	−1.42	38.89	48.10	+0.02
Si	6237.32	5.61	−1.10	60.06	70.13	+0.02
Si	6243.81	5.62	−1.27	46.56	56.90	+0.02
Si	6244.47	5.62	−1.29	46.69	58.14	+0.02
Ca	6156.02	2.52	−2.46	10.96	28.72	+0.01
Ca	6161.30	2.51	−1.29	65.28	103.61	+0.03
Ca	6166.44	2.51	−1.14	71.15	103.04	−0.02
Ca	6169.04	2.51	−0.80	91.31	125.18	−0.02
Ca	6455.60	2.51	−1.35	57.00	94.71	+0.02
Ca	6499.65	2.51	−0.82	83.98	120.18	−0.03
Sc II	5526.81	1.76	0.02	71.97	115.54	−0.18
Sc II	5640.97	1.49	−0.96	40.38	85.80	−0.08
Sc II	5657.87	1.50	−0.40	67.21	108.67	−0.13
Sc II	5669.03	1.49	−1.05	35.00	71.40	−0.22
Sc II	6245.63	1.51	−1.06	35.52	72.53	−0.17
Ti II	5211.53	2.59	−1.45	33.57	59.91	−0.03
Ti I	5219.70	0.02	−2.24	28.17	98.08	+0.02
Ti II	5418.77	1.58	−2.07	49.77	83.76	−0.10
Ti I	5648.57	2.50	−0.32	10.89	38.58	+0.03
Ti I	5662.16	2.32	−0.10	23.74	63.38	0.00
Ti I	6126.22	1.07	−1.38	22.67	83.01	0.00
V	5670.85	1.08	−0.45	21.11	84.83	+0.18
V	5737.07	1.06	−0.70	14.09	64.21	+0.03
V	6081.45	1.05	−0.70	14.88	69.13	+0.03
V	6274.66	0.27	−1.75	9.35	64.19	+0.03
V	6285.17	0.28	−1.65	10.83	70.82	+0.06
Cr	5287.18	3.44	−0.95	11.36	34.10	+0.10
Cr	5300.75	0.98	−2.09	59.85	113.35	−0.07
Cr	5783.07	3.32	−0.42	34.46	60.41	−0.06
Cr	5787.92	3.32	−0.15	48.21	78.27	−0.07
Mn	5399.47	3.85	−0.18	40.98	76.07	+0.04
Mn	5413.67	3.86	−0.65	25.25	52.05	+0.09
Co	5352.05	3.58	0.01	25.00	58.31	0.00
Co	5359.20	4.15	0.04	9.67	22.59	−0.08
Co	5647.24	2.28	−1.55	15.11	56.60	0.00
Ni	5625.32	4.09	−0.70	39.76	62.57	−0.10
Ni	5643.08	4.17	−1.24	16.63	31.66	−0.10
Ni	6086.29	4.27	−0.47	43.90	62.28	−0.16
Ni	6108.12	1.68	−2.51	67.40	121.27	−0.09
Ni	6111.08	4.09	−0.82	34.91	59.74	−0.02
Zn	4810.53	4.08	−0.22	76.37	81.34	−0.29
Y	5289.82	1.03	−1.88	4.25	23.86	+0.08
Y	5402.77	1.84	−0.58	12.65	40.71	+0.04
Zr	5112.27	1.67	−0.85	9.30	36.58	0.00
Ba	5853.67	0.60	−1.00	63.13	119.69	+0.18
Ba	6141.71	0.70	−0.08	114.63	117.42	+0.28
Ba	6496.90	0.60	−0.38	97.75	167.73	+0.28
La	6390.48	0.32	−1.46	3.31	30.67	+0.30
Nd	5311.45	0.99	−0.53	3.15	25.79	+0.28
Nd	5319.82	0.55	−0.34	12.00	60.83	+0.33
Eu	6645.10	1.38	0.22	6.14	28.67	+0.15

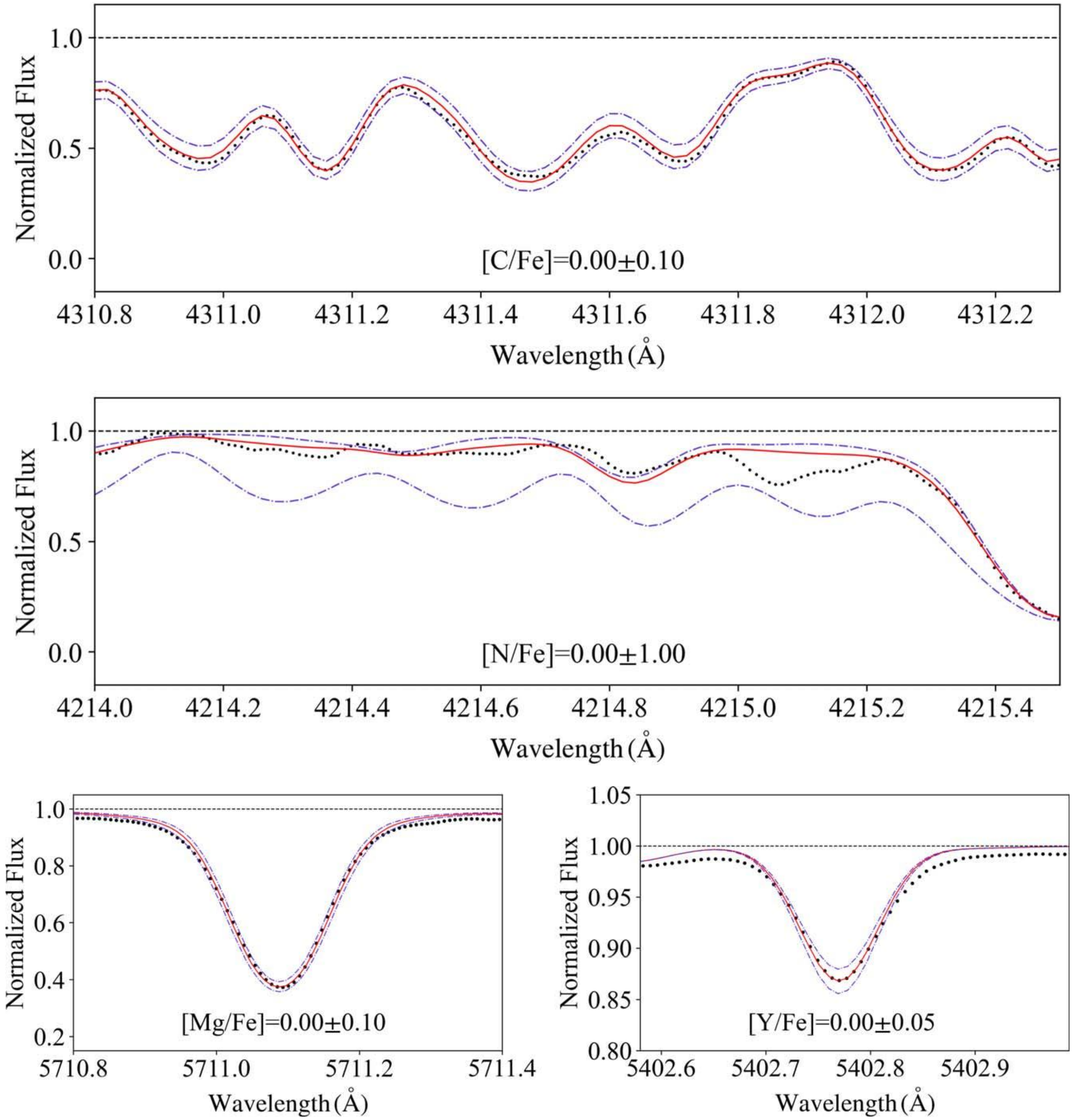

Figure A1. The synthetic line-fitting results (red solid line) of CH, CN, Mg, and Y in the observed solar spectrum (black dots). The solar atmospheric parameters are set to $T_{\mathrm{eff}} = 5777$ K, log $g = 4.44$, [Fe/H] = 0.00, and $v_{\mathrm{mic}} = 1.00$ km s^{-1}. The upper two panels show the CH and CN band with the observed solar spectrum taken by SOPHIE under HR mode, with abundance variations of 0.10 and 1.00 dex, respectively. Since molecular lines differ between dwarf and giant stars, the CN band is not well reproduced in the solar spectrum. The lower two panels show the fitting of Mg 5711 Å and Y 5402 Å lines with abundance variations of 0.10 and 0.05 dex, respectively.

ORCID iDs

Huiling Chen https://orcid.org/0009-0008-2988-2680
Yang Huang https://orcid.org/0000-0003-3250-2876
Wei Zhu https://orcid.org/0000-0003-4027-4711
Timothy C. Beers https://orcid.org/0000-0003-4573-6233
Renjing Xie https://orcid.org/0009-0002-4282-668X
Yutao Zhou https://orcid.org/0000-0002-4391-2822
Sharon Xuesong Wang https://orcid.org/0000-0002-6937-9034
Wei Wang https://orcid.org/0000-0002-9702-4441
Sofya Alexeeva https://orcid.org/0000-0002-8709-4665
Haozhu Fu https://orcid.org/0009-0002-4542-8046
Haining Li https://orcid.org/0000-0002-0389-9264
Lile Wang https://orcid.org/0000-0002-6540-7042
Huawei Zhang https://orcid.org/0000-0002-7727-1699

References

Aguilera-Gómez, C., Chanamé, J., Pinsonneault, M. H., & Carlberg, J. K. 2016, ApJL, 833, L24
Alexeeva, S., Ryabchikova, T., Mashonkina, L., & Hu, S. 2018, ApJ, 866, 153

Alexeeva, S., Wang, Y., Zhao, G., et al. 2023, ApJ, 957, 10
Blanco-Cuaresma, S. 2019, MNRAS, 486, 2075
Bland-Hawthorn, J., & Gerhard, O. 2016, ARA&A, 54, 529
Boothroyd, A. I., & Sackmann, I. J. 1999, ApJ, 510, 232
Bouchy, F., Hébrard, G., Udry, S., et al. 2009, A&A, 505, 853
Bovy, J. 2015, ApJS, 216, 29
Bressan, A., Marigo, P., Girardi, L., et al. 2012, MNRAS, 427, 127
Casamiquela, L., Soubiran, C., Jofré, P., et al. 2021, A&A, 652, A25
Charbonnel, C., Lagarde, N., Jasniewicz, G., et al. 2020, A&A, 633, A34
Chen, D.-C., Xie, J.-W., Zhou, J.-L., et al. 2021, ApJ, 909, 115
Chen, Y. Q., Nissen, P. E., Zhao, G., Zhang, H. W., & Benoni, T. 2000, A&AS, 141, 491
Döllinger, M. P., & Hartmann, M. 2021, ApJS, 256, 10
Gaia Collaboration, Vallenari, A., Brown, A. G. A., et al. 2023, A&A, 674, A1
GRAVITY Collaboration, Abuter, R., Amorim, A., et al. 2019, A&A, 625, L10
Grevesse, N., Asplund, M., & Sauval, A. J. 2007, SSRv, 130, 105
Gustafsson, B., Edvardsson, B., Eriksson, K., et al. 2008, A&A, 486, 951
Hatt, E., Nielsen, M. B., Chaplin, W. J., et al. 2023, A&A, 669, A67
Hon, M., Huber, D., Rui, N. Z., et al. 2023, Natur, 618, 917
Huang, Y., Beers, T. C., Wolf, C., et al. 2022, ApJ, 925, 164
Huang, Y., Liu, X. W., Yuan, H. B., et al. 2015, MNRAS, 449, 162
Huang, Y., Schönrich, R., Zhang, H., et al. 2020, ApJS, 249, 29
Huang, Y., Yuan, H., Beers, T. C., & Zhang, H. 2021a, ApJL, 910, L5
Huang, Y., Yuan, H., Li, C., et al. 2021b, ApJ, 907, 68
Kallinger, T., Beck, P. G., Stello, D., & Garcia, R. A. 2018, A&A, 616, A104
Kang, W., & Lee, S.-G. 2012, MNRAS, 425, 3162
Kumar, Y. B., Reddy, B. E., & Lambert, D. L. 2011, ApJL, 730, L12
Kunitomo, M., Ikoma, M., Sato, B., Katsuta, Y., & Ida, S. 2011, ApJ, 737, 66
Kurucz, R. L., Furenlid, I., Brault, J., & Testerman, L. 1984, National Solar Observatory Atlas (Sunspot, NM: National Solar Observatory)
Lee, B. C., Park, M. G., Lee, S. M., et al. 2015, A&A, 584, A79
Lindegren, L., Bastian, U., Biermann, M., et al. 2021, A&A, 649, A4
Masseron, T., Plez, B., Van Eck, S., et al. 2014, A&A, 571, A47
Mayor, M., & Queloz, D. 1995, Natur, 378, 355
Neves, V., Santos, N. C., Sousa, S. G., Correia, A. C. M., & Israelian, G. 2009, A&A, 497, 563
Nissen, P. E., Christensen-Dalsgaard, J., Mosumgaard, J. R., et al. 2020, A&A, 640, A81
Placco, V. M., Sneden, C., Roederer, I. U., et al. 2021, RNAAS, 5, 92
Reetz, J. K. 1991, PhD thesis, Universität München
Schlegel, D. J., Finkbeiner, D. P., & Davis, M. 1998, ApJ, 500, 525
Silva Aguirre, V., Ruchti, G. R., Hekker, S., et al. 2014, ApJL, 784, L16
Sitnova, T., Zhao, G., Mashonkina, L., et al. 2015, ApJ, 808, 148
Sitnova, T. M., Yakovleva, S. A., Belyaev, A. K., & Mashonkina, L. I. 2022, MNRAS, 515, 1510
Sneden, C., Bean, J., Ivans, I., Lucatello, S., & Sobeck, J. 2012, MOOG: LTE Line Analysis and Spectrum Synthesis, Astrophysics Source Code Library, ascl:1202.009
Spina, L., Meléndez, J., Karakas, A. I., et al. 2018, MNRAS, 474, 2580
Stello, D., Saunders, N., Grunblatt, S., et al. 2022, MNRAS, 512, 1677
Wolszczan, A., & Frail, D. A. 1992, Natur, 355, 145
Yan, H.-L., Zhou, Y.-T., Zhang, X., et al. 2021, NatAs, 5, 86
Yu, J., Huber, D., Bedding, T. R., et al. 2018, ApJS, 236, 42
Zhang, X., Jeffery, C. S., Li, Y., & Bi, S. 2020, ApJ, 889, 33
Zhao, G., Mashonkina, L., Yan, H. L., et al. 2016, ApJ, 833, 225
Zhou, Y., Li, X., Huang, Y., & Zhang, H. 2023, ApJ, 946, 73
Zhu, W., & Dong, S. 2021, ARA&A, 59, 291